Alzheimer's genetic risk factor *FERMT2* (Kindlin-2) controls axonal growth and synaptic plasticity in an APP-dependent manner

Fanny Eysert[1], Audrey Coulon[1], Emmanuelle Boscher[2,3], Anaïs-Camille Vreulx[1], Amandine Flaig[1], Tiago Mendes[1], Sandrine Hughes[4], Benjamin Grenier-Boley[1], Xavier Hanoulle[5], Florie Demiautte[1], Charlotte Bauer[6], Mikael Marttinen[7], Mari Takalo[7], Philippe Amouyel[1], Shruti Desai[1], Ian Pike[8], Mikko Hiltunen[7], Frédéric Chécler[6], Mélissa Farinelli[4], Charlotte Delay[1], Nicolas Malmanche[1], Sébastien Hébert[2,3], Julie Dumont[1], Devrim Kilinc[1], Jean-Charles Lambert[1,#] and Julien Chapuis[1, #]

[#] These authors share the last authorship

1. Univ. Lille, Inserm, CHU Lille, Institut Pasteur de Lille, U1167 - RID-AGE - Facteurs de risque et déterminants moléculaires des maladies liées au vieillissement, Lille 59019 France
2. Centre de recherche du CHU de Québec-Université Laval, CHUL, Axe Neurosciences, Québec, Canada
3. Faculté de médecine, Département de psychiatrie et de neurosciences, Université Laval, Québec, Canada
4. E-PHY-SCIENCE, Bioparc de Sophia Antipolis, 2400 route des Colles, Biot 06410 France
5. Univ. Lille, CNRS, UMR8576 - Labex DISTALZ, Villeneuve d'Ascq 59655 France
6. Université Côte d'Azur, Inserm, CNRS, IPMC, DistAlz Laboratory of Excellence, Valbonne, France
7. Institute of Biomedicine, University of Eastern Finland, Kuopio, Finland
8. Proteome Sciences plc, Hamilton House, London WC1H 9BB, United Kingdom

Corresponding author:

Julien Chapuis, PhD

Inserm UMR1167, Institut Pasteur de Lille, 1 rue du Pr. Calmette, Lille 59019 France

Tel: + 33 3 20 87 78 01

Fax: + 33 3 20 87 78 94

E-mail: julien.chapuis@pasteur-lille.fr

ABSTRACT

Although APP metabolism is being intensively investigated, a large fraction of its modulators are yet to be characterized. In this context, we combined two genome-wide high-content screenings to assess the functional impact of miRNAs and genes on APP metabolism and the signaling pathways involved. This approach highlighted the involvement of *FERMT2* (or Kindlin-2), a genetic risk factor of Alzheimer's disease (AD), as a potential key modulator of axon guidance; a neuronal process that depends on the regulation of APP metabolism. We found that FERMT2 directly interacts with APP to modulate its metabolism and that FERMT2 under-expression impacts axonal growth, synaptic connectivity and long-term potentiation in an APP-dependent manner. Lastly, the rs7143400-T allele, which is associated with an increased AD risk and localized within the 3'UTR of FERMT2, induced a down-regulation of FERMT2 expression through binding of miR-4504 among others. This miRNA is mainly expressed in neurons and significantly overexpressed in AD brains compared to controls. Altogether, our data provide strong evidence for a detrimental effect of FERMT2 under-expression in neurons and insight on how this may influence AD pathogenesis.

INTRODUCTION

AD is a neurodegenerative disease characterized by two main pathological hallmarks: (i) intracellular neurofibrillary tangles consisting of hyper-phosphorylated Tau proteins and (ii) extracellular amyloid plaques consisting of aggregates of β-amyloid (Aβ) peptides resulting from the processing of amyloid precursor protein (APP). Three main proteases (α-, β- and γ- secretases) are involved in APP processing through (i) the amyloidogenic pathway (β- and γ-secretases), leading to Aβ production, and (ii) the non-amyloidogenic pathway (α- and γ –secretases), which prevents Aβ generation by cleaving APP within the Aβ sequence (Checler 1995).

The identification of early-onset autosomal dominant AD-linked mutations in the genes for *APP* and presenilins (*PS1* and *PS2*, part of the γ-secretase), have placed abnormal APP metabolism at the center of the disease, further supporting the amyloid cascade hypothesis (Hardy 1997; Hardy & Selkoe 2002): the overproduction of Aβ peptides –especially the longer forms that are thought to be more neurotoxic– may lead to (or favor) Tau pathology and subsequent neuronal death.

Although the validity of the amyloid cascade hypothesis is debated (Morris et al. 2018), the importance of APP has recently been emphasized by the discovery of a rare *APP* mutation hampering Aβ production that lowers AD risk (Jonsson et al. 2012). Moreover, loss of functions variant in SORL1 (Sortilin-related receptor, L(DLR class A), which is a strong regulator of APP metabolism and Aβ production, is associated with early- and late-onset forms of AD (Nicolas et al. 2016; Andersen et al. 2005). Beyond Aβ production, the involvement of genetic risk factors such as APOE and TERM2 in modulation of Aβ aggregation and/or degradation/clearance has been proposed to be essential in the AD process (Kim et al. 2009; Jay et al. 2017). Recent high-throughput genomic approaches have also highlighted APP metabolism in the AD pathophysiological process: the main actors of APP metabolism, *e.g.*, ADAM10 and APH1B (part of the γ-secretase complex), have been characterized as genetic determinants (Jansen et al. 2019; Kunkle et al. 2019), and numerous other genetic determinants have been described as potential modulators of APP metabolism (for a review, see (Dourlen et al. 2019)).

Among these genetic determinants, FERMT2 has been identified to be involved in APP metabolism using an agnostic, systematic approach, *i.e.*, high content screening of 18,107 siRNA pools in HEK293 cells stably over-expressing an APP fusion protein (mCherry-APP^{695WT}-YFP) that allows for the quantification of intracellular APP fragments (Chapuis et al. 2017). Following this initial screening, FERMT2 under-expression was then specifically associated with increasing levels of mature APP at the cell surface, where FERMT2 facilitates APP recycling, resulting in increased Aβ peptide production (Chapuis et al. 2017).

Little is known about FERMT2. This protein localizes to focal adhesions, where it is proposed to interact with β3 integrin and to be a major actor in integrin activation (Theodosiou et al. 2016). FERMT2 has been reported as a key protein involved in cardiac and skeletal muscle development

80 (Dowling et al. 2008), and has been involved in cancer progression (Shen et al. 2012; Zhan et al. 2012;
81 Sossey-Alaoui et al. 2019). However, despite of the fact that FERMT2 is a major genetic risk factor of
82 AD, the physiological and/or pathophysiological roles of FERMT2 in the brain have not been
83 identified. Within this background, we sought to determine how FERMT2 regulation impacts APP
84 metabolism and/or AD risk and could be its involvement in neuronal functions.
85

86 **METHODS**

87

88 **Cell culture**

89 Human HeLa (RRID:CVCL_0030) and HEK293 (RRID:CVCL_0045) cells were respectively
90 maintained in Eagle's minimal essential medium (American Type Culture Collection, Teddington,
91 UK) and DMEM/Ham's F-12 1:1 medium (Life Technologies, Carlsbad, CA) supplemented with 10%
92 heat-inactivated fetal bovine serum and 2 mM L-glutamine, penicilline (10 UI/mL)/Streptomycine (10
93 µg/mL).

94

95 **Microfluidic chip fabrication**

96 Masters of multi-compartment microfluidic devices were fabricated through photolithography as
97 previously described (Blasiak et al. 2015). Polydimethylosiloxane (PDMS; Sylgard 184; Dow
98 Corning, Midland, MI) pads were replica molded (2 h at 70°C) and irreversibly bonded to glass
99 coverslips *via* O_2 plasma (Diener, Ebhausen, Germany). The devices were placed in plastic Petri
100 dishes, wetted with dH_2O, and UV sterilized for 30 min.

101

102 **Primary neuronal culture and viral transductions**

103 Primary neuronal cultures were obtained from hippocampus or cortices of post-natal (P0) rats as
104 described previously (Kaech & Banker 2006). Briefly, after the dissection of the brains, hippocampi
105 were washed three times in HBSS (HBSS, 1 M HEPES, penicilline/streptomycine, 100 mM sodium
106 pyruvate; Gibco) and were dissociated *via* trypsin digestion (2.5%, 37°C; Gibco) for 7 min. Next,
107 hippocampi were incubated with DNAse (5 mg/mL; Sigma) for 1 min and washed again in MEM
108 medium supplemented with 10% SVF, 1% Glutamax, 0.8% MEM vitamines, 0.5%
109 penicilline/streptomycine and 0.45% D-glucose (Sigma). With a pipette, hippocampi were
110 mechanically dissociated and resuspended in Neurobasal A medium (Gibco) supplemented with 2%
111 B27 (Gibco) and 0.25% GlutaMax. 200,000 neurons were seeded per well in 24-well plates. 50,000
112 neurons were seeded in the somatic chamber of microfluidic devices, pre-coated with poly-L-lysine
113 (0.1 mg/mL; Sigma) in borate buffer (0.31% boric acid, 0.475% sodium tetraborate, pH = 8.5). 0.1%
114 EDTA (in H_2O) was added to the Petri dishes containing microfluidic devices to minimize
115 evaporation. The culture medium was refreshed every 3 d. Neurons were maintained at 37°C in a
116 humidified 5% CO_2 incubator.

117

118 **Lentiviral transductions**

119 Lentiviral transductions were carried out at 1 day *in vitro* (DIV1) with a multiplicity of infection
120 (MOI) of 10. In the case of co-transduction, MOI of 5 was used for each lentivirus. Briefly,
121 lentiviruses were diluted in culture medium containing 4 µg/mL polybrene (hexadimethrine bromide;
122 Sigma) and were added to the cells. After 6 h of transduction, lentivirus suspension was replaced with

123 fresh medium. The following lentiviruses were used for transduction: Mission shRNA vectors (Sigma)
124 shNT (Non-Mammalian shRNA Control, SHC002), shFERMT2 (TRCN0000191859), shAPP
125 (TRCN0000006707) and pLenti6 empty vectors (Mock) or including human $FERMT2^{WT}$ or
126 $FERMT2^{QW}$ cDNA sequences. LifeAct-Ruby lentivirus (pLenti.PGK.LifeAct-Ruby.W:
127 RRID:Addgene_51009) was a kind gift from Rusty Lansford.
128
129 **RFLP genotyping**
130 Genomic DNA in the vicinity of the rs7143400 was amplified by PCR using the following primers 5'-
131 GGTTGGGTGTGAATAGGAAT-3' and 5'-TGCATGCCTGATTTATTTGG-3' before digestion
132 with Tsp45I enzyme (Thermo Scientific). Finally, treated PCR products were analyzed in 2% agarose
133 gel to visualize the cleavage bands.
134
135 **Designing CRISPR/Cas9 and genome editing**
136 gRNA sequences were predicted by Benchling (http://www.benchling.com) and cloned into the
137 GeneArt CRISPR OFP Nuclease Vector (ThermoFischer Scientific) allowing Cas9 and gRNA
138 expression. Homology directed repair was induced by co-transfection of 71 pb double-strained DNA
139 oligonucleotide template including rs7143400-T allele in HEK293 cells (**Supplementary Fig. 1**).
140 HEK293 clones were isolated by limiting dilution before RFLP genotyping. Sequence integrity of the
141 *FERMT2* 3'UTR and predicted potential off-target sites were validated by Sanger sequencing
142 (**Supplementary Fig. 1**).
143
144 **Visualization of miRNA expression at the single-cell level**
145 To visualize RNA molecules by fluorescence at single-cell resolution and quantify gene expression,
146 we used ViewRNA Cell Plus Assay kit (ThermoFischer Scientific) according to the manufacturer's
147 instructions. Briefly, after fixation and permeabilization, cells were washed 3× with PBS containing
148 RNAse inhibitor and were incubated with probes directed against specific mRNA or miRNA for 2 h at
149 40°C. After washes, probes were amplified, first, in a pre-amplifier solution and second, in an
150 amplifier solution, both for 1 h at 40°C. Then, cells were incubated with nucleotide probes stained
151 with different fluorophores allowing the detection of mRNA or miRNA puncta. This approach was
152 coupled with immunofluorescence experiments described.
153
154 **miRNA quantification in human brain samples**
155 This study was approved by CHU de Québec – Université Laval Research Ethics Committee (#2017-
156 3017). Frozen human brain tissue (0.5–1.2 g per sample) was obtained from the Harvard Brain Tissue
157 Resource Center in Belmont, USA, the Brain Endowment Bank in Florida, USA, and the Human
158 Brain and Spinal Fluid Resource Center in Los Angeles, USA, *via* NIH Neurobiobank. The cohort of
159 patients included non-dementia controls (N = 30) and AD cases (N = 52) based on neuropathological

160 diagnosis. Upon receipt of the specimens, frozen post-mortem parietal coxtex (BA39) was crushed
161 using a biopulverizer prior to RNA extraction and analysis.
162 Total RNA was extracted from brain tissue (**Supplementary Table 1**) using TRIzol reagent (Ambion,
163 15596018) according to the manufacturer's instructions. miRNA quantifications were done using the
164 TaqMan miR Reverse Transcription Kit (Applied Biosystem, Burlington, Canada) and TaqMan
165 Universal Master Mix (Applied Biosystem, 4324018) following the manufacturer's instructions.
166 Primers were purchased from ThermoFisher (miR-4504 ID: 464271_mat; RNU48 ID: 001006; miR-
167 222-3p ID: 002276). MiR-4504 and miR-222 levels were normalized to RNU48. The relative amounts
168 of each mature miRNA were calculated using the comparative Ct ($2^{-\Delta\Delta Ct}$) method (Smith et al. 2011).
169
170 **Immunoblotting and Aβ quantification**
171 Equal amounts (10-25 µg) of cell lysate were collected in RIPA buffer (1 M Tris, 1.5 M NaCl, 0.1%
172 NP-40, 10% SDS, 100 mM sodium orthovanadate, 0.5% sodium deoxycholate, pH = 7.4) containing
173 protease inhibitors (Complete mini; Roche Applied Science, Penzberg, Germany), lithium dodecyl
174 sulfate (LDS), and reducing agent (Invitrogen). Samples were denaturated and analyzed using SDS-
175 PAGE and the following antibodies: human FERMT2 (RRID:AB_10727911), amyloid precursor
176 protein C-terminal domain (RRID:AB_258409), actin (RRID:AB_476692), β-amyloid clone 6E10
177 (RRID:AB_662798), β-amyloid clone 4G8 (RRID:AB_662812), Synaptophysin I
178 (RRID:AB_887824), PSD95 (RRID:AB_2619800), GAPDH (RRID:AB_10615768). Extracellular
179 culture media were collected in order to dose secreted Aβ using Alpha-LISA assays (AlphaLISA
180 Amyloid β_{1-X} Kit, AL288C, PerkinElmer) according to the manufacturer's instructions.
181
182 **Cell surface biotinylation**
183 HEK293-APP^{695WT} cells were transfected with PCDNA4.1, $FERMT2^{WT}$ or $FERMT2^{QW}$
184 (PCDNA4/HisMax, ThermoScientific V86420) for 48 h. Next, cell surface proteins were biotinylated
185 using sulfo-NHS-SS-biotine (sulfosuccinimidyl-20(biotinamido)ethyl-1,3-dithiopropionate) for 30 min
186 at 4°C according to the manufacturer's instructions (Cell Surface Protein Isolation Kit, Pierce, 89881).
187 Then, cells were lysed and immunoprecipitated with streptavidin beads. Precipitated proteins were
188 eluted from the beads with loading buffer containing 50 mM DTT, heated for 10 min at 95°C and
189 analyzed by WB.
190
191 **Co-immunoprecipitation**
192 Equal amounts of protein were collected in co-immunoprecipitation buffer (10 mM HEPES, 140 mM
193 NaCl, 0.5% NP-40, pH = 7.4) containing protease inhibitors (Complete mini, Roche Applied Science)
194 and phosphatase inhibitor (100 mM sodium orthovanadate) and incubated with the primary β-amyloid
195 antibody clone 4G8 (RRID:AB_662812) overnight, with gentle rocking. Production of recombinant
196 C100 fragment was performed as previously described (Sevalle et al. 2009). Co-immunoprecipitation

197 was carried out using Pierce Protein A/G magnetic beads kit (Thermo Scientific, 88802) according to
198 the manufacturer's instructions. Samples with proteins and antibody complexes were incubated with
199 25 µL (0.25 mg) of A/G magnetic beads previously washed with co-immunoprecipitation buffer. After
200 1 h of incubation at 4°C, the magnetic beads were washed 3×, resuspended with loading buffer (LDS
201 and reducing agent) for 10 min at RT, and analyzed by WB.
202
203 **Immunofluorescence and PLA**
204 Cells were fixed in 4% paraformaldehyde (PFA) for 15 min, washed 3× with PBS, and permeabilized
205 for 5 min with 0.3% Triton X-100. Cells were incubated with 5% normal donkey serum for 2 h at RT
206 before overnight incubation with the following primary antibodies: human FERMT2
207 (RRID:AB_10727911), Kindlin2 (RRID:AB_2278298), amyloid precursor protein C-terminal domain
208 (RRID:AB_258409), APP A4 clone 22C11 (RRID:AB_94882), Synaptophysin I (
209 RRID:AB_887824), PSD95 (RRID:AB_2619800), Homer (RRID:AB_2631222), α-Tubulin
210 (RRID:AB_2210391). The cells were then washed 3× with PBS and incubated with the following
211 secondary antibodies raised in donkey (AlexaFluor-conjugated AffiniPure Fragment 405, 488, 594 or
212 647, Jackson ImmunoResearch), 1:10,000 Hoechst 33342, or 1/40 SiR-Actin probe (SC001,
213 Spirochrome). Alternatively, Kindlin2 (RRID:AB_2278298) and APP A4 22C11 (RRID:AB_94882)
214 antibodies were used for proximity ligation assay (PLA) according to manufacturer's instructions
215 (Duolink®, Olink Bioscience).
216
217 **Live-cell microscopy for axon elongation and actin dynamics**
218 After DIV5, once the axons reached the axonal chamber of microfluidic devices, the culture medium
219 was replaced with Neurobasal A without phenol red, supplemented with GlutaMax, 2% B_{27}, and 25
220 mM HEPES. Phase-contrast images of growing axons were acquired every 10 min for 110 min using
221 Zeiss AxioObserver Z1 microscope equipped with a Prime 95B Scientific CMOS (Photometrics,
222 Tucson,AZ) camera and 32× objective. Movies were analyzed using Fiji MTrack J Plugin (Meijering
223 et al. 2012) to determine the axon growth speed.
224 To visualize filamentous actin (F-actin) dynamics in the growth cones of elongating axons, neurons
225 were co-transducted with LifeAct-Ruby at DIV1. At DIV5, growth cones expressing LifeAct-Ruby
226 were imaged using a Nikon microscope equipped with Yokogawa spinning disk system and a Nikon
227 CFI Apochromat 100× TIRF objective (NA 1.49), in live superresolution mode (66 nm/px). Processed
228 movies were analyzed using Imaris (Bitplane, Zurich, Switzerland) surface tracking tool to obtain the
229 speed and direction of F-actin puncta undergoing actin retrograde flow.
230
231 **Synaptosome extraction**
232 To verify the presence of proteins at the synaptic level we did a subcellular fractionation as previously
233 described (Frandemiche et al. 2014). Briefly, cortical neurons were resuspended in a solution (0.32 M

234 sucrose and 10 mM HEPES, pH = 7.4) and were centrifuged at 1,000× *g* for 10 min to remove nuclei
235 and debris. The supernatant was centrifuged at 12,000× *g* for 20 min to remove the cytosolic fraction.
236 The pellet was resuspended in a second solution (4 mM HEPES, 1 mM EDTA, pH = 7.4) and was
237 centrifuged 2× at 12,000× *g* for 20 min. The new pellet was resuspended in a third solution (20 mM
238 HEPES, 100 mM NaCl, 0.5% Triton X-100, pH = 7.2) for 1 h at 4°C and centrifuged at 12,000× *g* for
239 20 min. The supernatant collected corresponds to the non-PSD fraction (Triton-soluble). The
240 remaining pellet was resuspended in a fourth solution (20 mM HEPES, 0.15 mM NaCl, 1% Triton X-
241 100, 1% deoxycholicacid, 1% SDS, pH = 7.5) for 1 h at 4°C and was centrifuged at 10,000× *g* for 15
242 min to obtain a supernatant containing the PSD fraction (Triton-insoluble). The different fractions
243 were then analyzed by WB.
244
245 **Quantification of synaptic connectivity**
246 To quantify synaptic connectivity, we transducted primary hippocampal neurons in pre- and/or
247 postsynaptic compartments of microfludic devices at DIV1 with lentiviruses carrying shNT and/or
248 shFERMT2 (MOI = 10). At DIV14 cultures were fixed and immunostained against Synaptophysin I
249 and Homer pre- and post-synaptic markers, respectively. Synaptic compartments were imaged with
250 Zeiss LSM880 confocal microscope, using a 63× 1.4 NA objective and the AiryScan superresolution
251 unit. Images were analyzed with Imaris software (Bitplane; Zürich, Switzerland) by reconstructing
252 Synaptophysin I and Homer puncta in 3D. The volume and position information of all puncta were
253 processed using a custom Matlab (MathWorks, Natick, MA) program. This program assigns each
254 postsynaptic spot to the nearest presynaptic spot (within a distance threshold of 1 μm) and calculates
255 the number of such assignments for all presynaptic puncta. The percentage of presynaptic spots not
256 assigned by any postsynaptic spot was consistently used as a read-out of synaptic connectivity.
257
258 **Lentivirus injection**
259 For stereotactic injections, C57Bl6/J mice (RRID:IMSR_JAX:000664) were anesthetized with 4%
260 isoflurane (2 L/min) and placed in a stereotaxic frame (68528, RWD Life Science, Shenzhen, China)
261 in which the head of the animal was fixed with a pair of ear bars and a perpendicular tooth bar. During
262 surgical procedures 1.5% isoflurane (2 L/min) was delivered through a facial mask *via* spontaneous
263 respiration. Their body temperature was maintained between 36.5 and 37.5°C with a homeothermic
264 blanket. Head was shaved and Vetedine was applied. Wounds and pressure points were infiltrated with
265 lidocaine. A skin incision was made along the sagittal midline of the scalp. Craniotomy was made to
266 target the structures of interest. Lentiviruses were injected in right and left hippocampus (1.5 μL per
267 hemisphere; 0.2 μL/min). After injections, wound clips were used for skin closure. For the sham
268 group, surgical procedures were performed without any injection. During the surgery, the level of
269 anesthesia was regularly verified by testing the nociceptive hind limb withdrawal reflex. Subjects were

270 then allowed to recover in their home cages for at least 7 d before sacrifice for ex-vivo
271 electrophysiological recordings.
272
273 **Hippocampal acute slices preparation**
274 One week after the surgery, sagittal hippocampal brain slices were obtained using standard brain
275 slicing methods. Mice were deeply anesthetized with isoflurane and decapitated. The brain was
276 quickly removed and immersed in ice-cold pre-oxygenated artificial cerebrospinal fluid (aCSF)
277 containing: 124 mM NaCl, 3.75 mM KCl, 2 mM $MgSO_4$, 2 mM $CaCl_2$, 26.5 mM $NaHCO_3$, 1.25 mM
278 NaH_2PO_4, and 10 mM Glucose and was continuously oxygenated (pH = 7.4; 27°C). 350 µm-thick
279 slices were prepared using a Vibratome (VT 1000S; Leica Microsystems, Bannockburn, IL), and
280 placed in a holding chamber filled with aCSF. Slices were allowed to recover in these conditions at
281 least 1 h before recording.
282
283 **Electrophysiological recordings**
284 For electrophysiological recordings, a single slice was placed in the recording chamber, submerged
285 and continuously superfused with gassed (95% O_2, 5% CO_2) aCSF at a constant rate (2 mL/min).
286 Extracellular fEPSPs were recorded in the CA1 stratum radiatum using a glass micropipette filled with
287 aCSF. fEPSPs were evoked by the electrical stimulation of Schaffer collaterals/commissural pathway
288 at 0.1 Hz with a glass stimulating electrode placed in the stratum radiatum (100 µsec duration).
289 To test the effect of miRNA-expressing lentiviruses on basal synaptic transmission, Input/Output (I/V)
290 curves were constructed at the beginning of the experiment. The slope of fEPSPs was measured and
291 plotted against different intensities of stimulation (from 0 to 100 µA).
292 Stable baseline fEPSPs were recorded by stimulating at 30% maximal field amplitude for 10 min prior
293 to the beginning of the experiment (single-pulse stimulation every 10 s (0.1 Hz). The same intensity of
294 stimulation was kept for the reminder of the experiment. For the paired-pulse facilitation (PPF)
295 protocol, two stimulations were applied with 50, 100, 150, 200, 300, 400 and 500 ms interval. For
296 long-term potentiation (LTP) protocol, after a 10 min stable baseline period, LTP was induced by the
297 following stimulation protocol: 3 trains of 100 stimulations at 100 Hz at the same stimulus intensity,
298 with 20 s intervals between trains. Following this conditioning stimulus, a 1 h test period was recorded
299 where responses were again elicited by a single-pulse stimulation every 10 s (0.1 Hz) at the same
300 stimulus intensity. Signals were amplified with an Axopatch 200B amplifier (Molecular Devices,
301 Union City, CA) digitized by a Digidata 1550 interface (Axon Instruments, Molecular Devices, San
302 Jose, CA) and sampled at 10 kHz. Recordings were acquired using Clampex (Molecular Devices) and
303 analyzed with Clampfit (Molecular Devices). Experimenters were blinded to treatment for all
304 experiments.
305
306

307 **RESULTS**

308

309 **FERMT2 expression is dependent on miRNAs modulating APP metabolism**

310 We used an unbiased screening approach to identify miRNAs that modulate APP metabolism in a
311 HCS model that allows for the quantification of intracellular APP fragments (Chapuis et al. 2017).
312 We screened a total of 2,555 mature human miRNAs in a 384-well plate format allowing us to identify
313 50 miRNAs (top and bottom 1%) with the strongest impact on APP metabolism (**Supplementary**
314 **Table 2** and **Supplementary Fig. 2**). To determine which genes were potentially regulated by these
315 top 50 hits, we selected the intersection of predictions resulting from at least four different algorithms
316 (see methods) and thereby identified 6,009 putative miRNA-target genes. To further refine the list of
317 predicted genes, we cross-checked them against a list of 832 genes that we previously identified to
318 have a major impact on APP metabolism in a genome-wide siRNA screening (Chapuis et al. 2017)
319 (**Supplementary Fig. 3**). This resulted in 180 common genes that are putative targets of 41 miRNAs.
320 To determine if any of these 180 genes were preferentially regulated by this pool of 41 miRNAs, we
321 performed 1 million drawing lots of 41 miRNAs among the 2,555 tested and compared them against
322 the list of miRNAs predicted to bind in the 3'-UTR of each of the 180 genes (**Supplementary Fig. 3**).
323 The AD genetic risk factor *FERMT2* (encoding Kindlin-2) was among the most significant genes (*p*-
324 value $< 2.77\times10^{-4}$ after Bonferroni correction) that strongly modulate APP metabolism, and whose
325 expression are potentially regulated by miRNAs that also strongly modulate APP metabolism.
326 According to our screening, four miRNAs were predicted to target FERMT2 3'UTR: miR-582-5p,
327 miR-200b-3p, miR-221-3p and miR-222-3p (**Fig. 1a**).

328

329 **miRNA-dependent FERMT2 expression and genetic variation associated with AD risk**

330 Our data indicate that regulation of the FERMT2 expression is dependent on miRNAs and we aimed
331 to assess whether genetic variations associated with AD risk may modulate the miRNA-dependent
332 expression of FERMT2. None of the variants localized within the FERMT2 3'-UTR were predicted to
333 modify the binding of miR-582-5p, miR-200b-3p, miR-221-3p, or miR-222-3p to this region
334 (Supplementary methods). In contrast, we had previously identified an AD-associated variant
335 (rs7143400), where the minor T allele creates an 8-mer binding site for miR-4504 within the 3'-UTR
336 of FERMT2 (Delay et al. 2016) (**Supplementary Fig. 4**). Supporting these predictions, we observed
337 that miR-4504 led to reduced luciferase expression only in the presence of *FERMT2* 3'UTR
338 rs7143400-T allele, whereas the four other miRNAs were able to induce a down-regulation regardless
339 of the rs7143400 allele (**Fig 1b**).

340 We then assessed the impact of these five miRNAs on endogenous FERMT2 expression levels after
341 their transfection in either $HEK293^{WT}$ or rs7143400-mutated HEK293 cell lines ($HEK293^{rs7143400\text{-}G/T}$)
342 generated by CRISPR-Cas9 technology (**Fig. 1c** and **Supplementary Fig. 1 and 5**). Accordingly,
343 transfection of miR-582-5p, miR-200b-3p, miR-221-3p, or miR-222-3p in HEK293 cells led to

344 reduced FERMT2 expression whatever their genotype while transfection of miR-4504 decreased the
345 endogenous FERMT2 expression only in the HEK293$^{rs7143400\text{-}G/T}$ cell line (**Fig. 1d** and **e**). Similar
346 effects were observed in HeLa cells that were genotyped to be heterozygous for rs7143400 (**Fig. 1c, d**
347 and **e and Supplementary Fig. 5**).
348
349 **Impact of miRNAs targeting FERMT2 on APP metabolism**
350 These five miRNAs are thus potential candidates to modulate APP metabolism through a direct down-
351 regulation of FERMT2. However, these miRNAs can also potentially target others genes strongly
352 modulating APP metabolism (**Supplementary Table 3**). We reasoned that if a candidate miRNA
353 affects APP metabolism mainly through down-regulating FERMT2, this candidate miRNA would
354 have similar effects on APP metabolism as the direct FERMT2 down-regulation by siRNAs we had
355 previously demonstrated, i.e. leading an increase of both intra- and extracellular byproducts of APP
356 (Chapuis et al. 2017). To investigate this hypothesis, we used the data generated in our HCS approach
357 (based on HEK293 cell line stably over-expressing a mCherry-APP695WT-YFP) in order to quantify
358 intracellular byproducts of APP (Sannerud et al. 2011; Chapuis et al. 2017) and we also measured Aβ
359 and sAPPα secretion after miR-582-5p, miR-200b-3p, miR-221-3p, or miR-222-3p transfections.
360 Only miR-582-5p and miR-222-3p showed similar effects as FERMT2 down-regulation (Chapuis et
361 al. 2017), *i.e.*, they increased the levels of intracellular APP metabolites tagged by mCherrry and YFP
362 and increased Aβ and sAPPα secretion (**Fig. 2a** and **b**).
363 Since the potential effects of miR-4504 would depend on the presence of the rs7143400 minor T
364 allele, we were not able to test for its impact in our HCS model. We nevertheless took advantage of
365 HEK293$^{rs7143400\text{-}G/T}$ cells by co-transfecting them with miR-4504 and mCherry-APP^{695WT}-YFP cDNA
366 in order to mimic our HCS model. When compared to HEK293$^{rs7143400\text{-}G/G}$, the transfection of miR-
367 4504 in HEK293$^{rs7143400\text{-}G/T}$ led to an accumulation of intracellular APP mCherry and YFP-tagged
368 metabolites and an increase of Aβ and sAPPα secretion (**Fig. 2c** and **d**). MiR-4504 showed similar
369 effects as FERMT2 down-regulation, and this observation further support that miR-4504 regulates
370 APP metabolism as a function of the FERMT2 rs7143400 variant.
371 In conclusion, we characterized that regulation of FERMT2 expression by miRNAs impacts APP
372 metabolism, and potentially in a genetics-dependent manner.
373
374 **miRNA expression in different hippocampal cell types and in AD brains**
375 To provide further physiological relevance to our findings, we first combined classical
376 immunocytochemistry with RNA hybridization which allows for the detection of miRNAs at single-
377 copy sensitivity. We observed that miR-200, miR-222 and miR-4504 were mainly expressed in
378 neurons when compared to astrocytes (**Fig. 3a**). We next measured the expression levels of these
379 miRNAs in the post-mortem brain samples from 52 AD patients and 30 control subjects. We observed
380 that the expression levels of miR-200 and miR-4504 were significantly higher in AD brains than in

381 controls (**Fig. 3b**). Collectively, these data suggest that endogenous FERMT2 expression and its
382 impact on APP metabolism are dependent on the expression of several miRNAs, two of which are
383 over-expressed in the brains of AD cases and, among these two, one impacts APP metabolism in the
384 presence of a genetic variant associated with AD risk.
385
386 **Pathway analyses suggest FERMT2/APP interaction to be involved in axonal growth**
387 Little is known about the physiological processes that require the regulation of APP expression and/or
388 its metabolism by miRNAs. To obtain a list of potential physiological pathways to be further
389 investigated, pathway enrichment analysis was performed using the 41 candidate miRNAs that
390 strongly modified APP metabolism in our HCS (**Supplementary Table 2**). This analysis revealed that
391 the candidate miRNAs are predicted to regulate neuronal pathways, such as axonal guidance (**Table**
392 **1a**). Since these 41 miRNAS potentially target 180 genes that strongly modulate APP metabolism
393 (**Supplementary Table 3**), we also performed pathway-enrichment analysis using these 180 genes.
394 This analysis revealed that these genes are predicted to be involved in axonal guidance among others
395 (**Table 1b**). In conclusion, both miRNAs and genes modulating APP metabolism, *e.g.*, FERMT2,
396 potentially play a role in axonal guidance.
397 APP is already known to be enriched in axonal growth cones during nervous system development and
398 acts as a co-receptor for axon guidance and cell migration cues through its interaction with the
399 extracellular matrix (Soldano & Hassan 2014) (Sosa et al. 2013). We thus investigated the potential
400 involvement of FERMT2 in axonal growth. Using primary neurons cultured in microfluidic devices
401 that fluidically isolate axons from their cell bodies, we first observed the co-localization of
402 endogenous FERMT2 with APP in the growth cones (**Fig. 4a**). We then addressed the impact of
403 FERMT2 silencing on axonal growth cone morphology using lentiviral vectors expressing either
404 shRNA against FERMT2 (shFERMT2) or a non-targeting shRNA (shNT). Actin staining revealed that
405 FERMT2 under-expression led to a significant decrease in growth cone area (9.13±0.71 vs 12.79±1.10
406 μm^2), as well as in the angular dispersion of growth cone filopodia during axonal growth (0.67±0.04
407 vs 0.84±0.02) (**Fig. 4b and Supplementary Fig. 6**). Of note, no significant impact on actin retrograde
408 flow rate was observed (0.166±0.003 vs 0.157±0.002 μm/s). These observations suggest a potential
409 impairment of the exploration behavior of the growth cones due to FERMT2 silencing, but not an
410 effect on actin dynamics *per se*. FERMT2 under-expression was also associated with an accumulation
411 of endogenous APP in the growth cones (1.38±0.11 vs 0.85±0.08, after normalization by the growth
412 cone area).
413 By performing proximity ligation assay (PLA), we observed PLA-FERMT2/APP signals in axonal
414 growth cones (**Fig. 4a**), suggesting a potential function of the FERMT2/APP complex in axon growth
415 behavior. To address this, we first tested the possibility that APP and FERMT2 form a protein-protein
416 complex *via* three complementary approaches: (i) Pull-down of endogenous APP from hippocampal
417 primary neuronal culture extracts co-immunoprecipitated endogenous FERMT2 (**Fig. 4c**). (ii) Over-

418 expression of FERMT2^{WT} was also able to pull-down the recombinant intracellular domain of APP
419 (**Fig. 4d**). (iii) In addition, we generated a $Q_{621}W_{622}AA$ FERMT2 mutant (FERMT2^{QW}) which was
420 previously shown to abolish the interaction between the FERMT2 F3 domain and the NxTY motif of
421 Integrin-β3 (which is also present within the intracellular domain of APP) (Ma et al. 2008).
422 Remarkably, when over-expressed in HEK293 cells, FERMT2^{QW} was not able to pull-down the
423 recombinant intracellular domain of APP. Cumulatively, these findings support a direct interaction
424 between FERMT2 and APP. Based on the recently solved crystal structure of FERMT2 in complex
425 with the integrin-β3-tail (Li et al. 2017), we built a structural model of the FERMT2/APP complex
426 (**Fig. 4e**), supporting our hypothesis that a protein-protein interaction exists between FERMT2 and
427 APP.
428 We next assessed the biological impact of the FERMT2/APP interaction on APP metabolism. By
429 performing extracellular biotinylation experiments, we observed that FERMT2 over-expression in
430 HEK293-APP^{695wt} cell line decreased the levels of APP at the cell surface, an effect that was abolished
431 by the presence of the QW mutation (**Fig. 4f**). Further, a dominant negative effect of the FERMT2^{QW}
432 mutant was observed: its over-expression impacted APP metabolism similarly to FERMT2 silencing,
433 *i.e.*, resulting in increased mature APP at the cell surface and increased Aβ production, as previously
434 reported (Chapuis et al. 2017). Altogether, our data suggest that a FERMT2/APP interaction is
435 necessary for FERMT2 to have an impact on APP metabolism.
436 In order to characterize in-depth the impact of FERMT2 and/or APP expression on axonal growth, we
437 conducted time-lapse microscopy and measured axon growth speed at DIV5 following lentiviral
438 transduction (shNT, shFERMT2, or shAPP) of neurons in microfluidic devices at DIV1. FERMT2
439 silencing led to 31.7% increase in axon growth speed (**Fig. 5 and Supplementary Fig. 6**). Conversely,
440 APP under-expression led to 16.7% decrease in axon growth speed. Remarkably, silencing of APP
441 was able to fully abolish the effect of FERMT2 under-expression on axon growth speed, suggesting
442 that APP was required for the molecular mechanism by which FERMT2 controls the axon growth
443 speed. In addition, we observed that FERMT2^{QW} mutant over-expression was able to induce 15.9%
444 increase in axon growth speed (**Fig. 5**). Since over-expression of FERMT2^{WT} did not show any
445 impact, these data also suggested a potential dominant negative effect of the FERMT2^{QW} mutant and
446 further supported the involvement of FERMT2/APP complex in axonal growth.
447
448 **FERMT2 is present at the synapse and controls synaptic connectivity**
449 Next, we investigated the impact of FERMT2 silencing on neuronal maturation at DIV14. First, co-
450 staining between FERMT2 and synaptic markers (Synaptophysin and Homer) suggested the
451 localization of FERMT2 at the synapse (**Fig. 6a**). The presence of FERMT2 in both pre- and
452 postsynaptic compartments was confirmed by synaptosomal purification (**Fig. 6b**). To control shRNA
453 expression separately in pre- or postsynaptic neurons, hippocampal neurons were cultured in
454 microfluidic devices that promote synapse formation in an isolated chamber (Taylor et al. 2010).

455 Thanks to the use of narrow microchannels, these devices spatially isolate neurites from their cell
456 bodies and allow lentiviral transductions to be conducted in different compartments, thereby allowing
457 us to silence FERMT2 expression at the pre- and/or postsynaptic levels (**Fig. 6c and Supplementary**
458 **Fig. 6**). The effects of shRNA expression (DIV1) on synaptic connectivity were assessed by confocal
459 microscopy of synaptic markers (DIV14) followed by three-dimensional image segmentation and
460 quantification. Under-expression of FERMT2 in the pre-synaptic chamber led to a decrease in synaptic
461 connectivity, whereas no such effect was observed when under-expressing FERMT2 in the post-
462 synaptic compartment (**Fig. 6d**). Altogether, our data suggest that FERMT2 expression is required for
463 synapse connectivity. Moreover, PLA-FERMT2/APP signals were co-localized with Synaptophysin
464 and Homer puncta (**Fig. 6e**), supporting the possibility of the involvement of the FERMT2/APP
465 complex in synapses.
466
467 **FERMT2 expression regulates synaptic plasticity in an APP dependent manner**
468 We sought to establish the functional impact of FERMT2 and/or APP silencing on paired-pulse
469 facilitation (PPF) and long-term potentiation (LTP) in *ex vivo* mouse (10-week-old male) hippocampal
470 slices, after stereotactic lentivirus injection allowing for the expression of shNT, shFERMT2, shAPP,
471 or shFERMT2+shAPP.
472 Broadly speaking, PPF arises due to increased presynaptic Ca^{2+}, which leads to the release of
473 neurotransmitter in two distinct waves. In this situation, two action potentials in the presynaptic cell
474 produce two excitatory postsynaptic potentials (EPSPs) in the postsynaptic cell: the first action
475 potential produces a first EPSP, but the second action potential produces an EPSP that is larger than
476 the EPSP produced by the first. PPF modulation therefore highlights a modulation in presynaptic
477 neurotransmitter release (Gebhardt et al. 2019). Using this read-out as a proxy for presynaptic
478 function, we observed a significant decrease in PPF in shFERMT2-infected mice compared to shNT-
479 infected control mice (**Fig. 7a**). This PPF impairment however was rescued when APP was also down-
480 regulated (shAPP+shFERMT2 group).
481 In separate experiments, tetanic stimulation was delivered to the Shaffer collaterals (SC) in order to
482 induce LTP in hippocampal slices (**Fig. 7b**). Tetanic stimulation of the SC resulted in a robust, long-
483 lasting potentiation of the field excitatory postsynaptic potential (fEPSP) slope in slices from mice
484 infected with shNT and with shAPP, whereas LTP was impaired in slices from shFERMT2-infected
485 mice. This suggests that an LTP deficit was observed in hippocampal slices infected with shFERMT2,
486 but not in those infected with shAPP (**Fig. 7c** and **7d**). Remarkably, this deficit was abolished when
487 both APP and FERMT2 were silenced, suggesting that APP was required for the molecular
488 mechanism by which FERMT2 impacts LTP.
489 Importantly, in these slices, no significant difference was observed for the normalized average slope of
490 the evoked fEPSP, indicating no alteration of the CA1 basal synaptic transmission occurred in any of
491 the groups analyzed (**Fig. 7e, Supplementary Fig. 7**).

492 Altogether, these data are in agreement with our previous observations that FERMT2 is involved in
493 the pre-synaptic compartment and modulates synaptic connectivity in an APP-dependent manner.
494

495 **DISCUSSION**

496

497 As in other multifactorial diseases, GWAS in AD are agnostic approaches, and how a genetic risk
498 factor is implicated in pathophysiological processes is typically unknown. Sometimes, even the
499 physiological functions of an AD genetic risk factor in the brain are not known. Understanding the
500 role of these genes is thus a challenge that requires several key questions to be addressed: (i) Does the
501 corresponding protein interact (directly or indirectly) with other key players and pathways known to
502 be involved in AD? (ii) What is (are) the functional variant(s) responsible for the GWAS signal and
503 does this (do these) variant(s) impact the biological function of the corresponding protein and its
504 interaction with key players of AD?
505 To answer these questions, we developed systematic approaches to determine the genes that are
506 involved in APP metabolism, a major player in AD development. To this end, we had previously
507 developed an HCS, based on the quantification of intracellular APP fragments, to measure the impact
508 of under-expression of 18,107 genes (*via* siRNA pools) on APP metabolism (Chapuis et al. 2017). In
509 the current study, we screened the impact of the over-expression of 2,555 miRNAs on APP
510 metabolism with the hypothesis that genes (i) that modulate the APP metabolism and (ii) whose
511 expression levels are regulated by miRNAs that also modulate the APP metabolism are likely some of
512 the key actors controlling the APP metabolism and functions. The convergence of these two agnostic
513 screens highlighted FERMT2, a GWAS-defined genetic risk factor of AD, for which almost nothing is
514 known in the cerebral and AD contexts.
515 We demonstrated that a direct interaction between FERMT2 and APP –through the F3 domain of
516 FERMT2 and the NxTY motif within APP's intracellular domain– is necessary for FERMT2 to have
517 an impact on APP metabolism. Moreover, we observed that the FERMT2/APP interaction could be
518 involved in the regulation of axonal growth, in line with APP's function within the growth cone (Sosa
519 et al. 2013) (data we replicated in this study). It has been reported that FERMT2 is required for the
520 recruitment and activation of focal adhesion kinase and the triggering of integrin signaling
521 (Theodosiou et al. 2016). In neurons, the focal adhesion pathway is involved in synaptic density and
522 activity through regulating the dendritic spine shape, stability, and the signalling machinery therein
523 (Hotulainen & Hoogenraad 2010). That is why we also analyzed synaptic plasticity, a read-out highly
524 relevant to AD, where synaptic dysfunction/loss is one of the earliest events observed. FERMT2
525 under-expression had detrimental effects on PPF (presynaptic) and LTP (postsynaptic). Remarkably,
526 in both cases, the detrimental effect of FERMT2 under-expression was dependent on APP expression.
527 In this context, it is important to note that numerous evidence indicate that presynaptic physiological

528 functions involving APP, which has been recently proposed as a structural and functional regulator of
529 the hippocampal presynaptic active zone (Weingarten et al. 2017), could be major molecular players in
530 AD (Barthet & Mulle 2020). As FERMT2 silencing leads to an accumulation of full-length APP and
531 all its by-products (including Aβ peptides), we can hypothesize that these accumulations could be
532 involved in the synaptic dysfunction observed due to FERMT2 under-expression, although further
533 experiments are needed to decipher the potential causal link between FERMT2 and APP, *i.e.*, to
534 determine whether FERMT2 impacts the function of full-length APP or invokes Aβ synaptotoxicity.
535 This is of particular interest, since APP shedding strongly enhances its cell adhesion and synaptogenic
536 activity (Stahl et al. 2014). Moreover, APP's intracellular domain is required for normal synaptic
537 morphology and synaptic plasticity, suggesting that its intracellular interaction partners could be
538 required for proper synaptic function (Klevanski et al. 2015). Remarkably, we have recently proposed
539 a circular model of AD pathogenesis, where the core of the focal adhesion pathway –which FERMT2
540 and APP are part of– may participate in the dysfunction of synaptic plasticity in AD (Dourlen et al.
541 2019).
542 We have also identified that *FERMT2* expression level is highly regulated by miRNAs which could be
543 preferentially expressed in neurons. In addition, we previously identified the rs7143400 variant located
544 in *FERMT2* 3'UTR to be susceptible to alter a binding site for miR-4504 (Delay et al. 2016). Here, in
545 addition to *in silico* prediction suggesting the impact of this variant on miRNA binding
546 (**Supplementary Fig. 4**), we demonstrate that this variant is functional: the AD-associated rs7143400
547 T allele down-regulates *FERMT2* and modulates APP metabolism *via* its interaction with miR-4504.
548 Remarkably, we observed that miR-4504 is over-expressed in the brains of AD cases compared to
549 controls, and is mainly expressed in neurons in primary mixed hippocampal cultures.
550 Together, our data indicate that a deleterious over-expression of miR-4504 can lead to a decrease in
551 FERMT2 expression in individuals bearing the rs7143400 minor T allele, which subsequently
552 modulates APP metabolism. Interestingly, similar mechanism has been reported for genetic variant
553 associated with AD risk in APP 3'UTR which regulates APP expression through miRNA binding (G
554 et al. 2016). Supporting a link between FERMT2 and APP metabolism, studies from cohorts of
555 patients have reported an association between variants in *FERMT2* gene and Aβ in CSF (Chapuis et al.
556 2017) and brain amyloidosis (Apostolova et al. 2018).
557 Here, we propose that FERMT2 down-regulation at the earliest stage of AD would depend in part on
558 (i) the miR-4504 expression, (ii) cerebral cell type (*i.e.*, neurons), and (iii) the presence of the
559 rs7143400 minor T allele (observed in 9% of Caucasians). Unfortunately, it is important to keep in
560 mind that all these constraints will make difficult, if not impossible, to detect such a miRNA-
561 dependent decrease in FERMT2 mRNA levels. Of note, this point may also underline the limitation of
562 expression databases in deciphering the mechanisms underlying the functional effects of GWAS
563 variants, for they do not allow capturing (even hide) subtle mechanisms.

564 In publicly-available RNA-seq analyses (Mayo Clinic Brain Bank), an over-expression of FERMT2
565 mRNA has been observed in post-mortem human temporal cortex of AD patients relative to healthy
566 controls (Sullivan et al. 2018). Even though a small sample size did not allow us to observe such a
567 variation in FERMT2 mRNA levels, we nevertheless detected an increase in FERMT2 protein levels
568 as a function of Braak stage, especially at later stages (**Supplementary Fig. 8)**. This point is of
569 particular importance since in the Genotype-Tissue Expression Database (GTEx Consortium et al.
570 2015), FERMT2 variants associated with an increase in AD risk at the genome-wide significance level
571 are also part of an expression quantitative trait locus, significantly associated with decreased brain
572 expression of FERMT2 mRNA (sentinel variant in GWAS rs17125924; −18%; p-value = 2×10^{-6}). Of
573 note, there is a strong linkage disequilibrium between rs7143400 and the GWAS hit rs17125924 (R^2 =
574 0.78) and rs7143400 has a lower Minor Allele Frequency (MAF = 0.09) and subsequently lower
575 association (p = 7.14×10^{-5}) than rs17125924 (MAF = 0.20; p = 6.6×10^{-7}). Altogether, these results
576 strongly support the notion that FERMT2 down-regulation is deleterious at the earliest stages of the
577 disease, whereas FERMT2 over-expression may occur as a pathological consequence at a later stage.
578 In conclusion, we propose that FERMT2 under-expression through miRNAs and/or genetic regulation
579 leads to synaptic dysfunction in an APP-dependent manner. Our hypothesis may thus call for new
580 therapeutic approaches in AD targeting FERMT2 and/or APP function, rather than Aβ peptide
581 production/clearance.

Acknowledgements

F. E. benefited from a doctoral grant co-funded by Hauts-de-France Regional Council and Institut Pasteur de Lille. The authors thank the BICeL and EquipEx ImagInEx HCS platforms of the Institut Pasteur de Lille and Alexandre Vandeputte for technical assistance. The authors thank Karine Blary at the IEMN Lille for the microfabrication work. This work was partly supported by the French RENATECH network. This study was funded by INSERM, Institut Pasteur de Lille, the Centres of Excellence in Neurodegeneration-ANR program (CoEN, GWAS in AD: focus on microRNA), the Canadian Institute of Health Research (CHIR), la Fondation Alzheimer (Syn-Alz), the EU Joint Programme – Neurodegenerative Diseases Research (JPND; 3DMiniBrain) and Fondation Vaincre Alzheimer (FR-17006p). This work was also funded by the Lille Métropole Communauté Urbaine and the French government's LABEX DISTALZ program (development of innovative strategies for a transdisciplinary approach to Alzheimer's disease). This work was supported for M.H by Academy of Finland (grant number 307866), Sigrid Jusélius Foundation and the Strategic Neuroscience Funding of the University of Eastern Finland. The authors thank the vectorology platform Transbiomed for lentivirus production.

Author contributions

J.-C. L. and J. C. designed and supervised research. A. F., F. E., F. C. and C. B. performed APP metabolism and FERMT2/APP interaction analyses. X. H. developed in silico model for FERMT2/APP interaction. F. E. and D. K. performed and analyzed axon growth experiments. A. C., A. F., J. D. and J. C. developed Crispr/Cas9 model and/or performed subsequent analyses. C. D., A.-C. V., A. F. and B. G.-B. designed and/or performed miRNA screening and/or statistical analyses. S. H. and M. F. performed and analyzed electrophysiology experiments. A. F., T. M., F. D. and S. D. performed primary neuronal cultures. M. M., M. T., I. P. and M. H. analyzed transcriptomic and/or proteomic data of FERMT2 expression in brains. E. B. and S. S. H. performed miR expression quantification in brains. F. E., N. M., D. K. and J. C. participated in image acquisition and analyses of APP/FERMT2 interaction and/or synapse density. F. E., P. A., J. D., D. K., J.-C. L. and J. C. wrote and/or revised the paper.

Conflicts of interest

S. H. and M. F. are full-time employees of E-Phy-Science SA. C. D. has been an employee of Janssen Pharmaceutica since her departure from the laboratory Inserm U1167 in 2016.

615 **References**

616 Andersen, O.M. et al., 2005. Neuronal sorting protein-related receptor sorLA/LR11 regulates
617 processing of the amyloid precursor protein. *Proceedings of the National Academy of Sciences of*
618 *the United States of America*, 102(38), pp.13461–6. Available at:
619 http://www.pnas.org/cgi/doi/10.1073/pnas.0503689102 [Accessed January 4, 2017].

620 Apostolova, L.G. et al., 2018. Associations of the Top 20 Alzheimer Disease Risk Variants With Brain
621 Amyloidosis. *JAMA Neurology*, 75(3), p.328. Available at:
622 http://www.ncbi.nlm.nih.gov/pubmed/29340569 [Accessed April 27, 2018].

623 Barthet, G. & Mulle, C., 2020. Presynaptic failure in Alzheimer's disease. *Progress in neurobiology*,
624 p.101801. Available at: http://www.ncbi.nlm.nih.gov/pubmed/32428558 [Accessed July 10,
625 2020].

626 Blasiak, A., Lee, G.U. & Kilinc, D., 2015. Neuron Subpopulations with Different Elongation Rates
627 and DCC Dynamics Exhibit Distinct Responses to Isolated Netrin-1 Treatment. *ACS chemical*
628 *neuroscience*, 6(9), pp.1578–90. Available at:
629 http://pubs.acs.org/doi/10.1021/acschemneuro.5b00142 [Accessed September 11, 2019].

630 Chapuis, J. et al., 2017. Genome-wide, high-content siRNA screening identifies the Alzheimer's
631 genetic risk factor FERMT2 as a major modulator of APP metabolism. *Acta Neuropathologica*,
632 133(6), pp.955–966. Available at: http://www.ncbi.nlm.nih.gov/pubmed/27933404 [Accessed
633 August 19, 2019].

634 Checler, F., 1995. Processing of the beta-amyloid precursor protein and its regulation in Alzheimer's
635 disease. *Journal of neurochemistry*, 65(4), pp.1431–44. Available at:
636 http://www.ncbi.nlm.nih.gov/pubmed/7561836 [Accessed July 13, 2016].

637 Delay, C. et al., 2016. miRNA-dependent target regulation: functional characterization of single-
638 nucleotide polymorphisms identified in genome-wide association studies of Alzheimer's disease.
639 *Alzheimer's research & therapy*, 8(1), p.20. Available at:
640 http://www.ncbi.nlm.nih.gov/pubmed/27215977 [Accessed June 17, 2016].

641 Dourlen, P. et al., 2019. The new genetic landscape of Alzheimer's disease: from amyloid cascade to
642 genetically driven synaptic failure hypothesis? *Acta neuropathologica*, 138(2), pp.221–236.
643 Available at: http://link.springer.com/10.1007/s00401-019-02004-0 [Accessed August 23, 2019].

644 Dowling, J.J. et al., 2008. Kindlin-2 is an essential component of intercalated discs and is required for
645 vertebrate cardiac structure and function. *Circulation research*, 102(4), pp.423–31. Available at:
646 http://www.ncbi.nlm.nih.gov/pubmed/18174465 [Accessed January 26, 2015].

647 Frandemiche, M.L. et al., 2014. Activity-dependent tau protein translocation to excitatory synapse is
648 disrupted by exposure to amyloid-Beta oligomers. *The Journal of neuroscience : the official*
649 *journal of the Society for Neuroscience*, 34(17), pp.6084–97. Available at:
650 http://www.ncbi.nlm.nih.gov/pubmed/24760868 [Accessed April 29, 2014].

651 G, N. et al., 2016. Mutation in the 3'untranslated Region of APP as a Genetic Determinant of Cerebral
652 Amyloid Angiopathy. *European journal of human genetics : EJHG*, 24(1). Available at:
653 https://pubmed.ncbi.nlm.nih.gov/25828868/ [Accessed June 16, 2020].

654 Gebhardt, C. et al., 2019. Priming of LTP in amygdala and hippocampus by prior paired pulse
655 facilitation paradigm in mice lacking brain serotonin. *Hippocampus*, 29(7), pp.610–618.
656 Available at: http://www.ncbi.nlm.nih.gov/pubmed/30457189 [Accessed July 10, 2020].

GTEx Consortium, K.G. et al., 2015. Human genomics. The Genotype-Tissue Expression (GTEx) pilot analysis: multitissue gene regulation in humans. *Science (New York, N.Y.)*, 348(6235), pp.648–60. Available at: http://www.sciencemag.org/cgi/doi/10.1126/science.1262110 [Accessed September 3, 2019].

Hardy, J., 1997. Amyloid, the presenilins and Alzheimer's disease. *Trends in neurosciences*, 20(4), pp.154–9. Available at: http://www.ncbi.nlm.nih.gov/pubmed/9106355 [Accessed November 2, 2016].

Hardy, J. & Selkoe, D.J., 2002. The amyloid hypothesis of Alzheimer's disease: progress and problems on the road to therapeutics. *Science.*, %19;297(5580), pp.353–356.

Hotulainen, P. & Hoogenraad, C.C., 2010. Actin in dendritic spines: connecting dynamics to function. *The Journal of cell biology*, 189(4), pp.619–29. Available at: http://www.jcb.org/lookup/doi/10.1083/jcb.201003008 [Accessed November 18, 2019].

Jansen, I.E. et al., 2019. Genome-wide meta-analysis identifies new loci and functional pathways influencing Alzheimer's disease risk. *Nature Genetics*, 51(3), pp.404–413. Available at: http://www.ncbi.nlm.nih.gov/pubmed/30617256 [Accessed September 4, 2019].

Jay, T.R. et al., 2017. Disease Progression-Dependent Effects of TREM2 Deficiency in a Mouse Model of Alzheimer's Disease. *The Journal of neuroscience : the official journal of the Society for Neuroscience*, 37(3), pp.637–647. Available at: http://www.ncbi.nlm.nih.gov/pubmed/28100745 [Accessed July 8, 2020].

Jonsson, T. et al., 2012. A mutation in APP protects against Alzheimer's disease and age-related cognitive decline. *Nature*, 488(7409), pp.96–99. Available at: http://www.nature.com/doifinder/10.1038/nature11283.

Kaech, S. & Banker, G., 2006. Culturing hippocampal neurons. *Nature protocols*, 1(5), pp.2406–15. Available at: http://www.nature.com/articles/nprot.2006.356 [Accessed September 19, 2019].

Kim, J., Basak, J.M. & Holtzman, D.M., 2009. The role of apolipoprotein E in Alzheimer's disease. *Neuron*, 63(3), pp.287–303. Available at: http://www.ncbi.nlm.nih.gov/pubmed/19679070 [Accessed July 8, 2020].

Klevanski, M. et al., 2015. The APP Intracellular Domain Is Required for Normal Synaptic Morphology, Synaptic Plasticity, and Hippocampus-Dependent Behavior. *Journal of Neuroscience*, 35(49), pp.16018–16033. Available at: http://www.ncbi.nlm.nih.gov/pubmed/26658856 [Accessed January 31, 2017].

Kunkle, B.W. et al., 2019. Genetic meta-analysis of diagnosed Alzheimer's disease identifies new risk loci and implicates Aβ, tau, immunity and lipid processing. *Nature Genetics*, 51(3), pp.414–430. Available at: http://www.ncbi.nlm.nih.gov/pubmed/30820047 [Accessed July 12, 2019].

Li, H. et al., 2017. Structural basis of kindlin-mediated integrin recognition and activation. *Proceedings of the National Academy of Sciences of the United States of America*. Available at: http://www.ncbi.nlm.nih.gov/pubmed/28739949 [Accessed July 31, 2017].

Ma, Y.-Q. et al., 2008. Kindlin-2 (Mig-2): a co-activator of beta3 integrins. *The Journal of cell biology*, 181(3), pp.439–46. Available at: http://www.pubmedcentral.nih.gov/articlerender.fcgi?artid=2364684&tool=pmcentrez&rendertype=abstract [Accessed October 15, 2014].

698 Meijering, E., Dzyubachyk, O. & Smal, I., 2012. Methods for cell and particle tracking. *Methods in*
699 *enzymology*, 504, pp.183–200. Available at:
700 https://linkinghub.elsevier.com/retrieve/pii/B9780123918574000094 [Accessed September 11,
701 2019].

702 Morris, G.P., Clark, I.A. & Vissel, B., 2018. Questions concerning the role of amyloid-β in the
703 definition, aetiology and diagnosis of Alzheimer's disease. *Acta Neuropathologica*, 136(5),
704 pp.663–689. Available at: http://www.ncbi.nlm.nih.gov/pubmed/30349969 [Accessed September
705 4, 2019].

706 Nicolas, G. et al., 2016. SORL1 rare variants: a major risk factor for familial early-onset Alzheimer's
707 disease. *Molecular Psychiatry*, 21(6), pp.831–836. Available at:
708 http://www.ncbi.nlm.nih.gov/pubmed/26303663 [Accessed April 21, 2017].

709 Sannerud, R. et al., 2011. ADP ribosylation factor 6 (ARF6) controls amyloid precursor protein (APP)
710 processing by mediating the endosomal sorting of BACE1. *Proceedings of the National Academy*
711 *of Sciences of the United States of America*, 108(34), pp.E559–68. Available at:
712 http://www.pubmedcentral.nih.gov/articlerender.fcgi?artid=3161548&tool=pmcentrez&renderty
713 pe=abstract [Accessed May 23, 2013].

714 Sevalle, J. et al., 2009. Aminopeptidase A contributes to the N-terminal truncation of amyloid beta-
715 peptide. *Journal of neurochemistry*, 109(1), pp.248–56. Available at:
716 http://doi.wiley.com/10.1111/j.1471-4159.2009.05950.x [Accessed October 8, 2019].

717 Shen, Z. et al., 2012. Kindlin-2: a novel adhesion protein related to tumor invasion, lymph node
718 metastasis, and patient outcome in gastric cancer. *American journal of surgery*, 203(2), pp.222–
719 9. Available at: http://linkinghub.elsevier.com/retrieve/pii/S0002961011005964 [Accessed April
720 27, 2018].

721 Smith, P.Y. et al., 2011. MicroRNA-132 loss is associated with tau exon 10 inclusion in progressive
722 supranuclear palsy. *Human molecular genetics*, 20(20), pp.4016–24. Available at:
723 https://academic.oup.com/hmg/article-lookup/doi/10.1093/hmg/ddr330 [Accessed September 2,
724 2019].

725 Soldano, A. & Hassan, B. a., 2014. Beyond pathology: APP, brain development and Alzheimer's
726 disease. *Current Opinion in Neurobiology*, 27, pp.61–67. Available at:
727 http://dx.doi.org/10.1016/j.conb.2014.02.003.

728 Sosa, L.J. et al., 2013. Amyloid precursor protein is an autonomous growth cone adhesion molecule
729 engaged in contact guidance. *PloS one*, 8(5), p.e64521. Available at:
730 http://www.pubmedcentral.nih.gov/articlerender.fcgi?artid=3653867&tool=pmcentrez&renderty
731 pe=abstract [Accessed October 24, 2014].

732 Sossey-Alaoui, K. et al., 2019. The Kindlin2-p53-SerpinB2 signaling axis is required for cellular
733 senescence in breast cancer. *Cell Death & Disease*, 10(8), p.539. Available at:
734 http://www.ncbi.nlm.nih.gov/pubmed/31308359 [Accessed January 10, 2020].

735 Stahl, R. et al., 2014. Shedding of APP limits its synaptogenic activity and cell adhesion properties.
736 *Frontiers in cellular neuroscience*, 8, p.410. Available at:
737 http://www.ncbi.nlm.nih.gov/pubmed/25520622 [Accessed January 11, 2017].

738 Sullivan, S.E. et al., 2018. Candidate-based screening via gene modulation in human neurons and
739 astrocytes implicates FERMT2 in Aβ and TAU proteostasis. *Human Molecular Genetics*.

740 Available at: https://academic.oup.com/hmg/advance-article/doi/10.1093/hmg/ddy376/5145655
741 [Accessed October 30, 2018].

742 Taylor, A.M. et al., 2010. Microfluidic local perfusion chambers for the visualization and
743 manipulation of synapses. *Neuron*, 66(1), pp.57–68. Available at:
744 http://www.ncbi.nlm.nih.gov/pubmed/20399729 [Accessed October 12, 2016].

745 Theodosiou, M. et al., 2016. Kindlin-2 cooperates with talin to activate integrins and induces cell
746 spreading by directly binding paxillin. *eLife*, 5. Available at:
747 http://www.pubmedcentral.nih.gov/articlerender.fcgi?artid=4749545&tool=pmcentrez&renderty
748 pe=abstract [Accessed February 4, 2016].

749 Weingarten, J. et al., 2017. APP-A Novel Player within the Presynaptic Active Zone Proteome.
750 *Frontiers in molecular neuroscience*, 10, p.43. Available at:
751 http://www.ncbi.nlm.nih.gov/pubmed/28265241 [Accessed July 10, 2020].

752 Zhan, J. et al., 2012. Opposite Role of Kindlin-1 and Kindlin-2 in Lung Cancers. *PLoS ONE*, 7(11),
753 pp.1–12.

754

755

756 **Table 1. Results of pathway enrichment analyses**

757 **a**. The 10 most likely canonical pathways identified after pathway enrichment analysis of 41 miRNAs
758 that strongly modulate APP metabolism using DIANA Tools mirPath (v3.0)

KEGG pathway	*p*-value	#miRNAs
Axon guidance	4.70E-08	48
Proteoglycans in cancer	1.82E-06	49
Hippo signaling pathway	4.10E-06	50
Fatty acid biosynthesis	8.10E-05	11
Glutamatergic synapse	8.56E-05	48
GABAergic synapse	1.10E-04	48
AMPK signaling pathway	2.20E-04	46
TGF-beta signaling pathway	2.50E-04	45
Thyroid hormone signaling pathway	3.90E-04	48
Adrenergic signaling in cardiomyocytes	5.00E-04	49

759

760 **b**. The 10 most likely canonical pathways identified after pathway enrichment analysis of 132 genes
761 targeted by 41 miRNAs (see Supplementary Methods for details)

KEGG pathway	*p*-value	#genes
Axon guidance	0.0014	19
Ubiquitin mediated proteolysis	0.010	16
Circadian rhythm	0.036	8

762

763

764

765

766 **Fig. 1. Validation of functional miRNAs targeting *FERMT2* 3'UTR**

767 **a.** Relative positions of miRNA target sites on *FERMT2* 3'UTR. The target site created by the
768 rs7143400-T allele, which is associated with AD risk, is shown in red. **b.** Luciferase activity of
769 FERMT2 3'UTR carrying either the rs7143400-G or the rs7143400-T allele in HEK-293 cells co-
770 transfected with a non-targeting miRNA (miR-NT) or 5 miRNA mimics. Data are expressed relative
771 to the miR-NT **c.** RFLP genotyping of HeLa and HEK293 cell lines edited or not for the rs7143400
772 *via* CRISPR-Cas9 (**Supplementary Fig. 1**). **d.** Endogenous FERMT2 expression levels were assessed
773 by Western blot using indicated cell extracts following transient transfection with a non-targeting miR
774 (miR-NT) or with the indicated miR for 72 h. **e.** WB quantifications from three independent
775 experiments as in ***d***. Data given in mean ± SD. * $p < 0.05$, non-parametric test compared to miR-NT
776 condition.

777

778 **Fig 2. Validation of the effects of FERMT2-targeting miRNA on APP metabolism**

779 **a.** Mean fluorescence intensity of intracellular mCherry and YFP signals obtained after miRNA
780 transfection in HEK293 cells stably over-expressing a mCherry-APP^{695WT}-YFP. **b.** Quantification of
781 Aβ and sAPPα secretion after miRNAs transfection in HEK293 cells stably over-expressing a
782 mCherry-APP^{695WT}-YFP. **c.** Mean fluorescence intensity variation of intracellular mCherry and YFP
783 signal obtained after miRNA transfection in HEK293$^{rs7143400\text{-}G/G}$ or HEK293$^{rs7143400\text{-}G/T}$ cell lines
784 transiently over-expressing a mCherry-APP^{695WT}-YFP. **d**. Quantification of Aβ and sAPPα secretion
785 after miRNAs transfection in HEK293$^{rs7143400\text{-}G/G}$ or HEK293$^{rs7143400\text{-}G/T}$ cell lines transiently over-
786 expressing a mCherry-APP^{695WT}-YFP. Bar charts show mean ± SD. Mann–Whitney test; * $p < 0.05$.

787

788 **Fig. 3. miRNA expression in primary neuronal cultures and in AD brains**

789 **a.** Hybridization experiments in rat postnatal hippocampal neuronal cultures enabling single-copy
790 detection of miRNA combined with immunocytochemistry against astrocytic (SOX9) and neuronal
791 (NeuN) markers. Scale bar = 20 µm. The box plot shows the quantification of miRNA copy number in
792 SOX9- or NeuN-positive cells (N > 30 cells for each condition). Black rectangles and red plus signs
793 indicate sample mean and outliers, respectively. **b.** Relative miRNA expression levels in temporal
794 lobes of non-demented (CTL) and AD groups. Mann–Whitney test; **** $p < 0.0001$.

795

796 **Fig 4. FERMT2 directly interacts with APP**

797 **a.** Immunofluorescence images showing the presence of APP and FERMT2 within the axonal growth
798 cone stained with SiR-Actin. The right panel shows the presence of PLA-FERMT2/APP puncta within
799 the axonal growth cone. **b.** Impact of lentiviral transduction of non-targeting shRNA (shNT) or
800 shRNA against FERMT2 (shFERMT2) on growth cone area, angular dispersion and speed of the actin

801 retrograde flow, and APP immunostaining. **c.** Co-IP between endogenous APP and FERMT2 from
802 membrane extracts of hippocampal PNC. Protein extracts were incubated with beads only, a mouse
803 (Ms) antibody against APP (4G8) or a non-relevant (NR) antibody. **d.** APP pull-down experiment with
804 wild type (WT) or mutated (QW) FERMT2. Protein extracts from HeLa cells overexpressing
805 $FERMT2^{WT}$ or $FERMT^{QW}$ were incubated with recombinant APP C-terminal fragment (C100). **e.** The
806 domain organization of FERMT2 protein (upper panel). Q614A/W615A (QW) mutation was reported
807 to abolish the interaction of F3 domain of FERMT2 with the NxTY motif. The structural model of the
808 FERMT2-APP complex (lower panel) was built by homology using the crystal structure of the
809 FERMT2-Integrin-β3-tail complex (Li et al. 2017). **f.** The impact of FERMT2 on APP metabolism in
810 HEK293-APP^{695WT} cells is reverted with the overexpression of $FERMT2^{QW}$ compared to $FERMT2^{WT}$.
811 Scale bar = 5 µm. Mann–Whitney test; * $p < 0.05$.
812
813 **Fig 5. FERMT2 regulates axonal growth rate depending on APP expression**
814 Impact of lentiviral transduction on axonal growth speed. Individual axon tracks from a representative
815 set are plotted. Scale bars = 50 µm. Box plots and cumulative distribution plots are color-matched. n is
816 the number of axons analyzed from at least three independent experiments. Kruskal-Wallis ANOVA
817 with multiple comparisons; * $p < 5\times10^{-3}$; *** $p < 5\times10^{-7}$.
818
819 **Fig 6. FERMT2 is present at the synapse and controls synaptic connectivity**
820 **a.** Immunofluorescence in hippocampal primary neuronal culture showing the co-localization of
821 FERMT2 puncta with pre- and postsynaptic markers, Synaptophysin and Homer, respectively. **b.**
822 Synaptic fractionation experiment revealed the presence of FERMT2 in both pre- and postsynaptic
823 compartments. **c**. Schematics of the tricompartmental microfluidic device. The use of microchannels
824 with different lengths ensures that only axons arrive from the presynaptic to the synaptic compartment,
825 where synapses can be observed independently of the cell bodies. The device also permits lentiviral
826 transductions to be performed exclusively in the pre- and postsynaptic compartments. **d.** Synaptic
827 connectivity as a function of FERMT2 under-expression in pre- and postsynaptic chambers. Increased
828 fraction of Synaptophysin spots not assigned by a Homer spot within a distance threshold of 1 µm is
829 indicative of decreased synaptic connectivity. **e.** PLA-FERMT2/APP puncta were observed at the
830 synapses stained for pre- and postsynaptic markers. Scale bars = 2 µm.
831
832 **Fig 7. FERMT2 under-expression alters PPF and LTP in an APP-dependent manner**
833 **a.** Paired-pulse facilitation (PPF) as a function of the interstimulus interval 7 days after viral injection
834 of indicated lentivirus. N = 3 mice; 2 slices per animal. **b.** Exemplary fEPSP traces during baseline
835 (light line) and 30-60 min after LTP induction (dark line). **c.** Time course of the average slope of
836 elicited fEPSP responses following LTP induction by a tetanic stimulation protocol in hippocampal
837 CA1 synapses after viral injection. Time-point 0 represents the delivery of the tetanic stimulation.

838 Slopes of each fEPSP are normalized by the baseline and plotted against time. **d.** Box plots of the
839 average slope response during 30-60 min post LTP induction. HFS: High frequency stimulation. N = 5
840 mice; 2 slices per animal. **e.** Normalized average slope of fEPSP evoked in hippocampal slices from
841 animals injected with the indicated lentivirus. Recordings have been performed in the stratum
842 radiatum of hippocampal CA1 region with electrical stimulation of Schaffer collaterals (see Methods).
843 Unpaired t-test; * $p < 0.05$; ** $p < 0.01$**.**
844

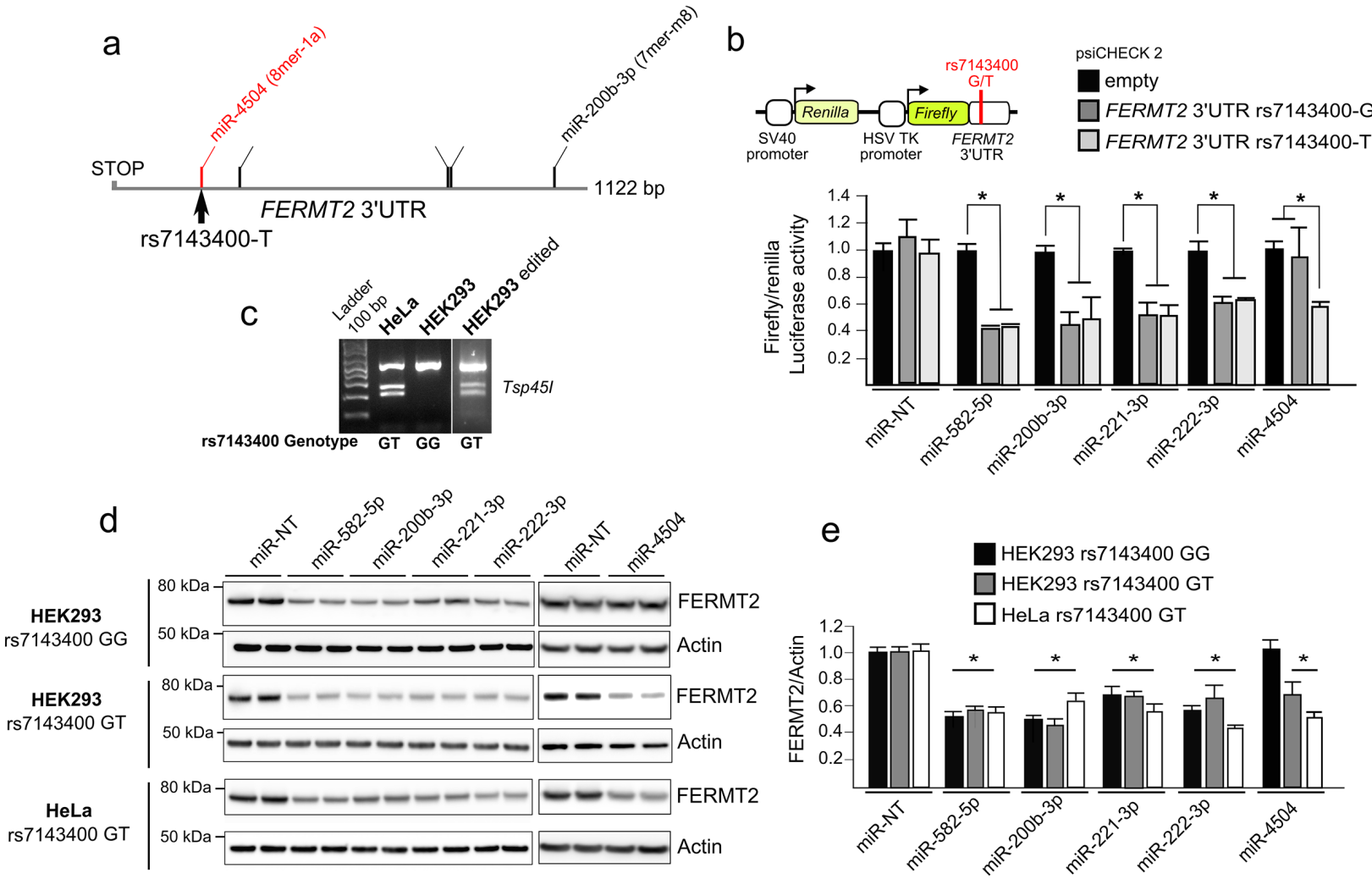
a
miR-4504 (8mer-1a)
miR-200b-3p (7mer-m8)
STOP
1122 bp
FERMT2 3'UTR
rs7143400-T
b
rs7143400
G/T
Renilla
Firefly
SV40 promoter
HSV TK promoter
FERMT2 3'UTR
psiCHECK 2
empty
FERMT2 3'UTR rs7143400-G
FERMT2 3'UTR rs7143400-T
Firefly/renilla Luciferase activity
miR-NT
miR-582-5p
miR-200b-3p
miR-221-3p
miR-222-3p
miR-4504
c
Ladder 100 bp
HeLa
HEK293
HEK293 edited
Tsp45I
rs7143400 Genotype
GT
GG
GT
d
miR-NT
miR-582-5p
miR-200b-3p
miR-221-3p
miR-222-3p
miR-NT
miR-4504
HEK293 rs7143400 GG
HEK293 rs7143400 GT
HeLa rs7143400 GT
80 kDa
50 kDa
FERMT2
Actin
e
HEK293 rs7143400 GG
HEK293 rs7143400 GT
HeLa rs7143400 GT
FERMT2/Actin

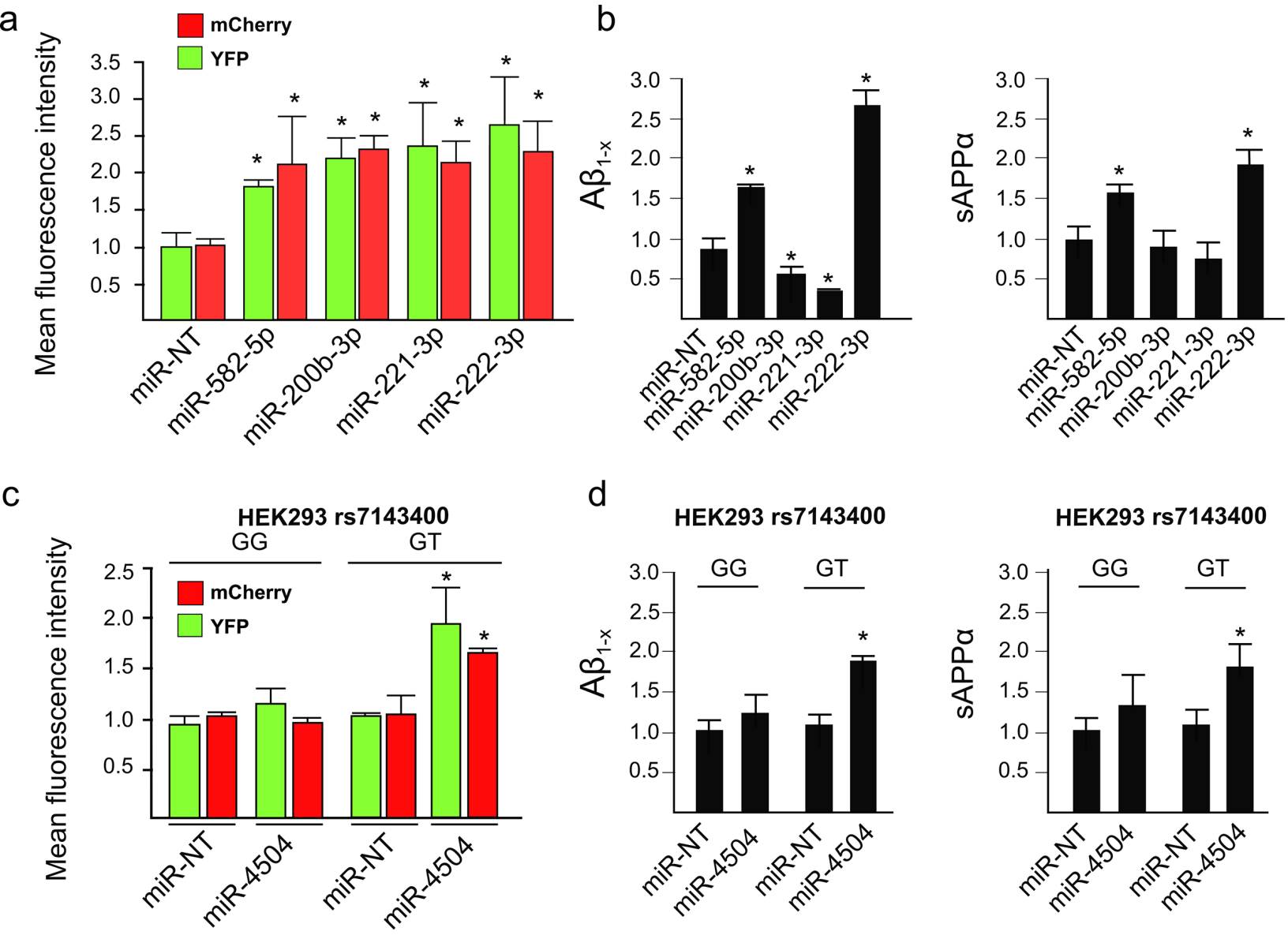
a
mCherry
YFP
Mean fluorescence intensity
3.5
3.0
2.5
2.0
1.5
1.0
0.5
miR-NT
miR-582-5p
miR-200b-3p
miR-221-3p
miR-222-3p
b
Aβ1-x
sAPPα
c
HEK293 rs7143400
GG
GT
miR-4504
d

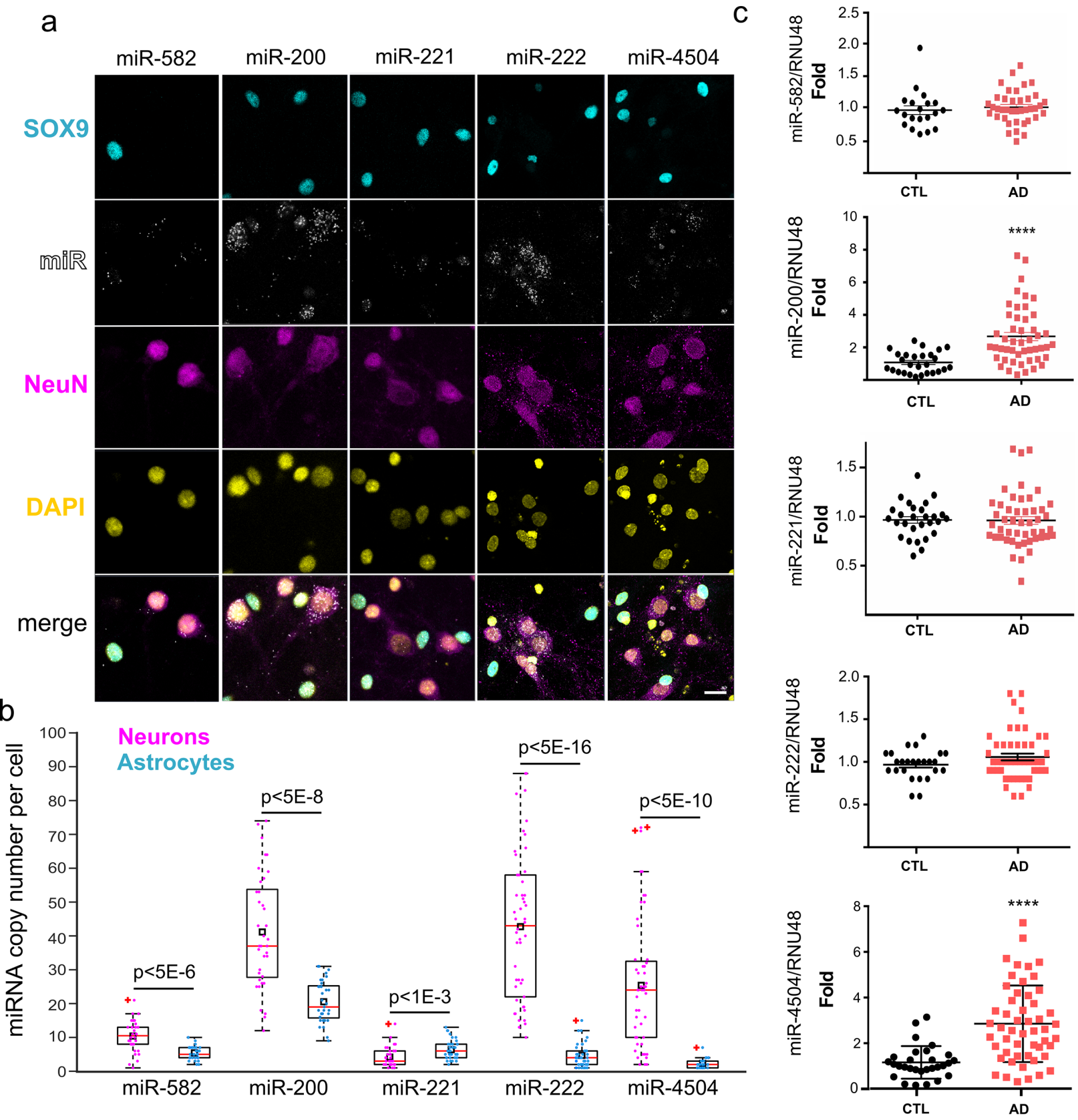
a
miR-582
miR-200
miR-221
miR-222
miR-4504
SOX9
miR
NeuN
DAPI
merge
b
Neurons
Astrocytes
miRNA copy number per cell
p<5E-6
p<5E-8
p<1E-3
p<5E-16
p<5E-10
miR-582
miR-200
miR-221
miR-222
miR-4504
c
miR-582/RNU48
miR-200/RNU48
miR-221/RNU48
miR-222/RNU48
miR-4504/RNU48
Fold
CTL
AD
****

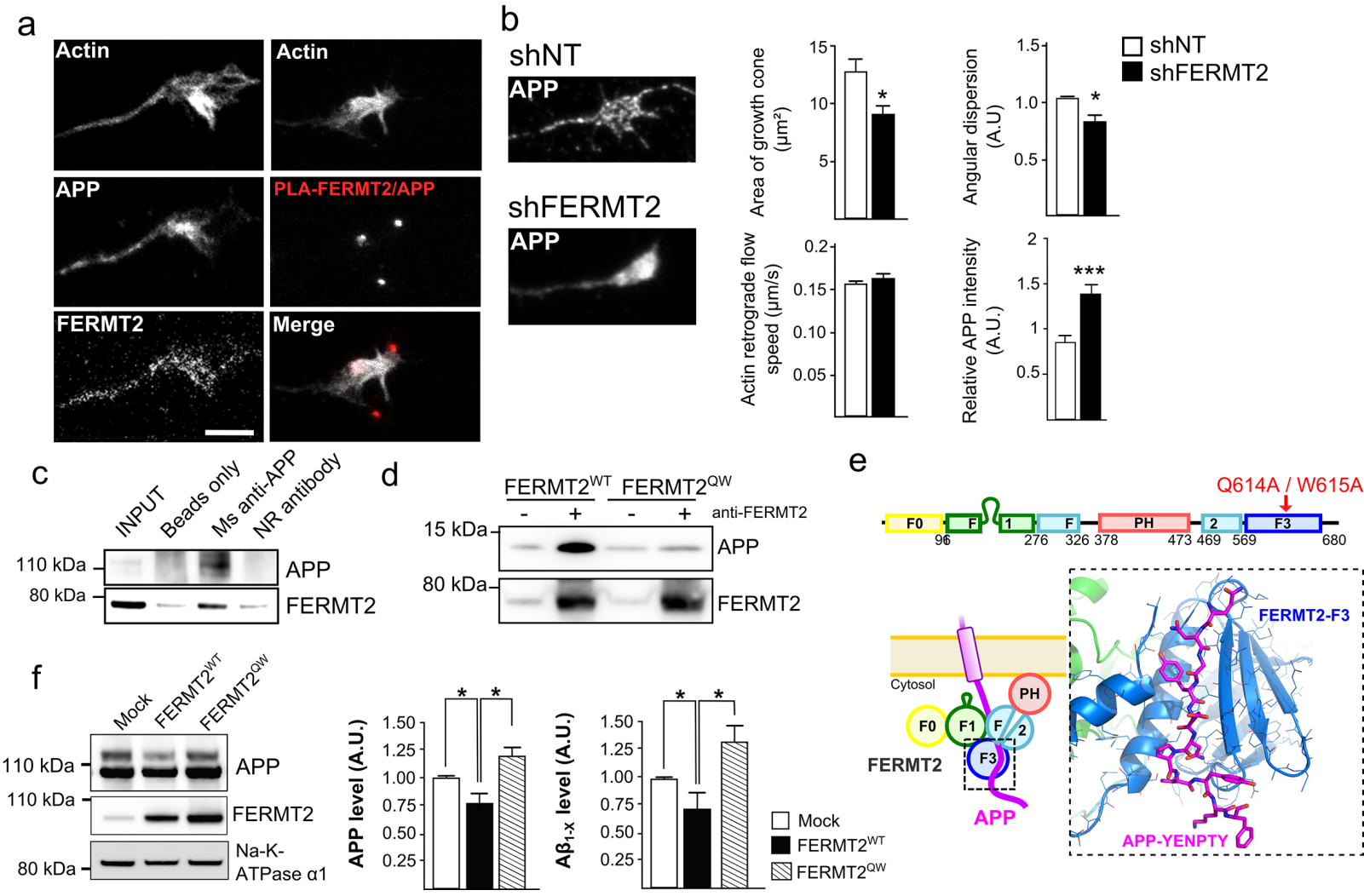
a
Actin
Actin
APP
PLA-FERMT2/APP
FERMT2
Merge
b
shNT
APP
shFERMT2
APP
Area of growth cone (µm²)
Angular dispersion (A.U)
Actin retrograde flow speed (µm/s)
Relative APP intensity (A.U.)
shNT
shFERMT2
c
INPUT
Beads only
Ms anti-APP
NR antibody
110 kDa
80 kDa
APP
FERMT2
d
FERMT2WT
FERMT2QW
anti-FERMT2
15 kDa
80 kDa
APP
FERMT2
e
Q614A / W615A
F0
F
1
F
PH
2
F3
96
276
326
378
473
469
569
680
Cytosol
PH
F0
F1
F
2
F3
FERMT2
APP
FERMT2-F3
APP-YENPTY
f
Mock
FERMT2WT
FERMT2QW
110 kDa
110 kDa
80 kDa
APP
FERMT2
Na-K-ATPase α1
APP level (A.U.)
Aβ1-x level (A.U.)
Mock
FERMT2WT
FERMT2QW

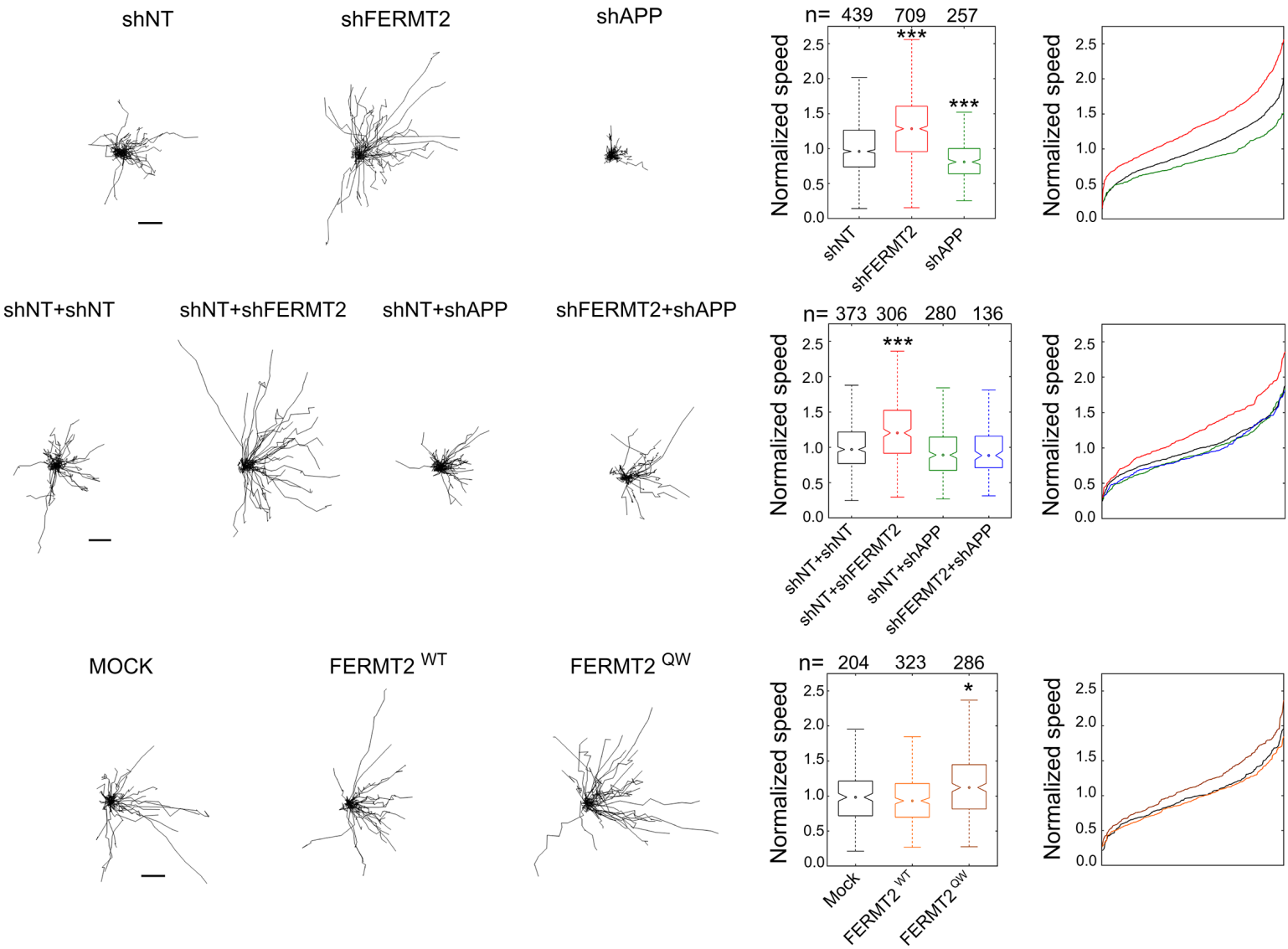
shNT
shFERMT2
shAPP
n= 439 709 257
Normalized speed
shNT
shFERMT2
shAPP
shNT+shNT
shNT+shFERMT2
shNT+shAPP
shFERMT2+shAPP
n= 373 306 280 136
MOCK
FERMT2 WT
FERMT2 QW
n= 204 323 286
Mock

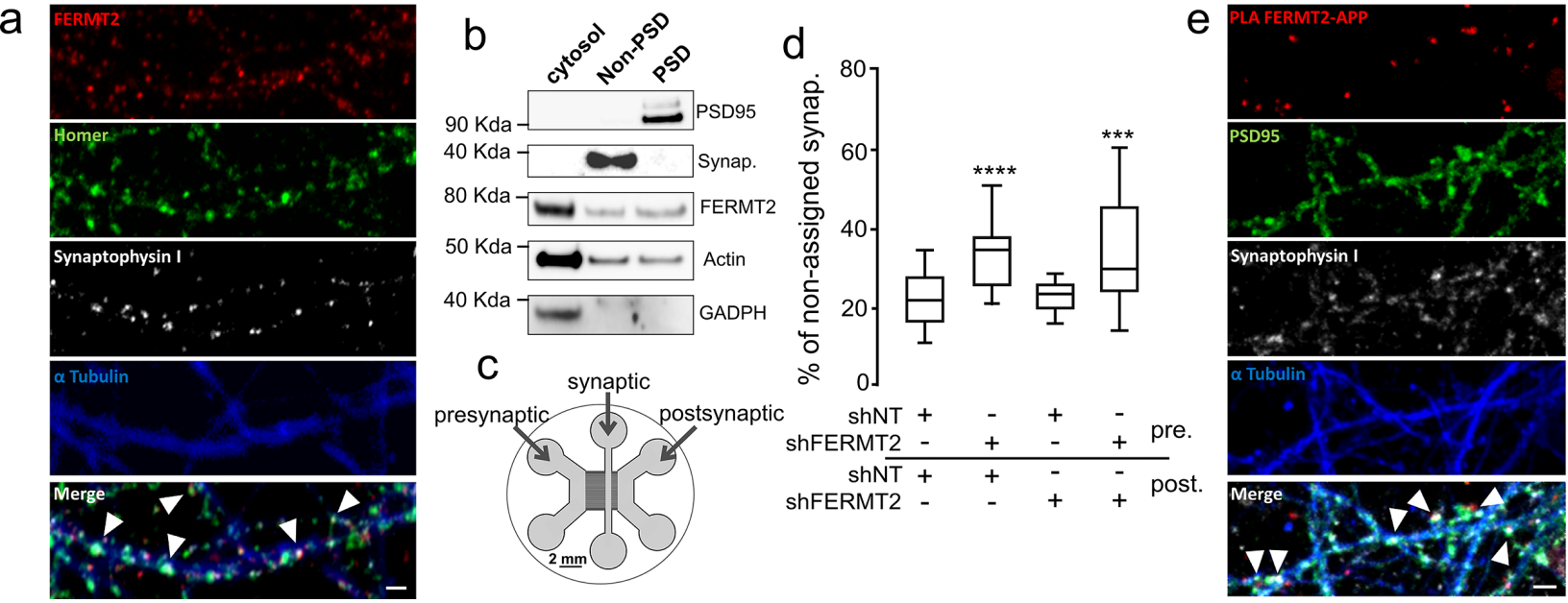
a
FERMT2
Homer
Synaptophysin I
α Tubulin
Merge
b
cytosol
Non-PSD
PSD
90 Kda
PSD95
40 Kda
Synap.
80 Kda
FERMT2
50 Kda
Actin
40 Kda
GADPH
c
synaptic
presynaptic
postsynaptic
2 mm
d
% of non-assigned synap.
80
60
40
20
0
****
***
shNT + - + -
shFERMT2 - + - +
pre.
shNT + + - -
shFERMT2 - - + +
post.
e
PLA FERMT2-APP
PSD95
Synaptophysin I
α Tubulin
Merge

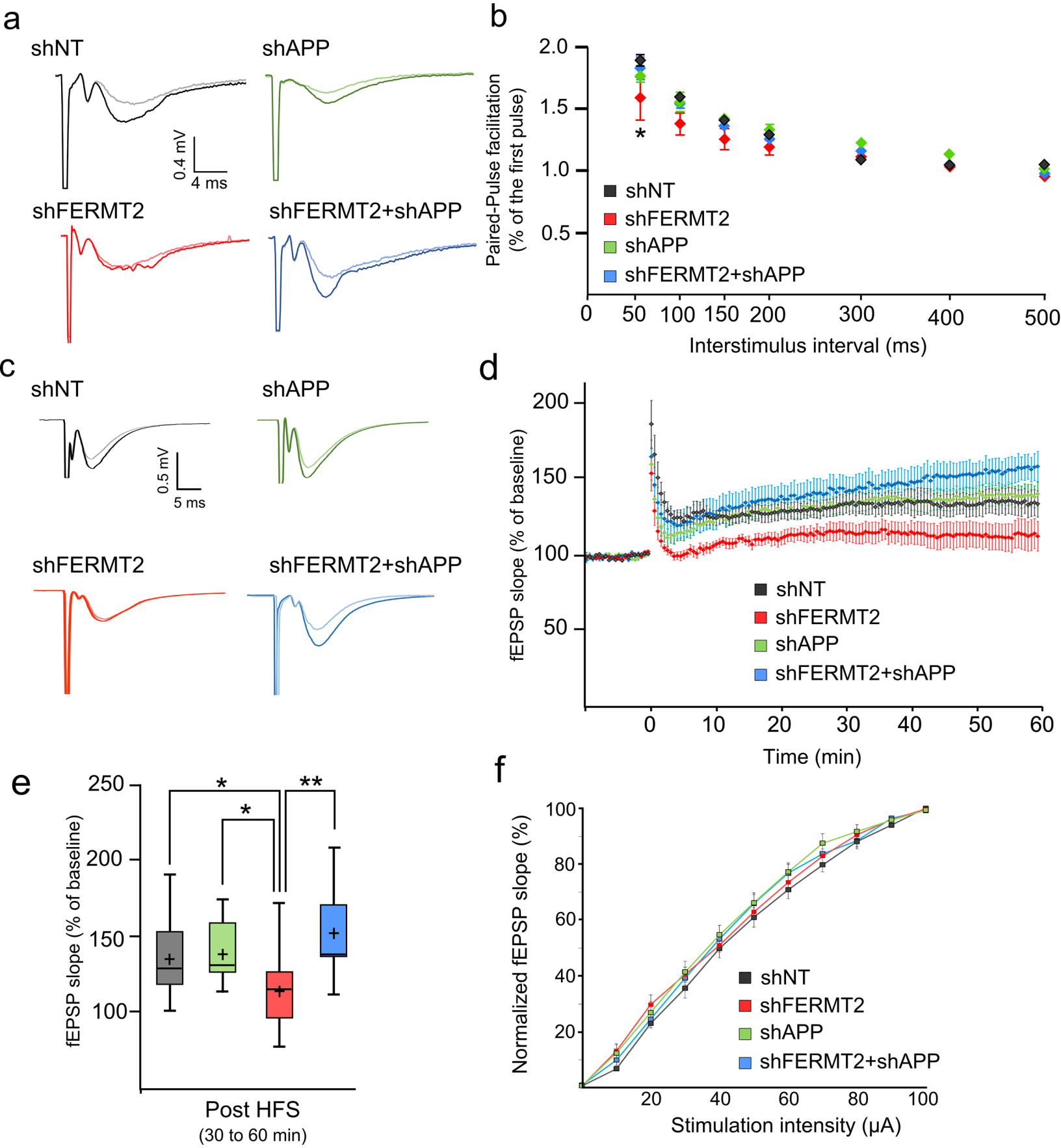
a
shNT
shAPP
0.4 mV
4 ms
shFERMT2
shFERMT2+shAPP
b
Paired-Pulse facilitation (% of the first pulse)
2.0
1.5
1.0
0.5
*
shNT
shFERMT2
shAPP
shFERMT2+shAPP
0
50
100
150
200
300
400
500
Interstimulus interval (ms)
c
shNT
shAPP
0.5 mV
5 ms
shFERMT2
shFERMT2+shAPP
d
fEPSP slope (% of baseline)
200
150
100
50
shNT
shFERMT2
shAPP
shFERMT2+shAPP
0
10
20
30
40
50
60
Time (min)
e
fEPSP slope (% of baseline)
250
200
150
100
*
*
**
Post HFS
(30 to 60 min)
f
Normalized fEPSP slope (%)
100
80
60
40
20
shNT
shFERMT2
shAPP
shFERMT2+shAPP
20
40
60
80
100
Stimulation intensity (μA)